

A parametric study on cave footprint capacity in discontinuous rock masses

S. Dehkoda^a and F. Reusch^b

^a Beck Engineering, Brisbane, Australia.

^b Beck Engineering, Berlin, Germany

ABSTRACT

Maintaining cave footprint stability during production necessitates a deep understanding of geological, geomechanical, and mining engineering factors that control cave initiation and establishment. This involves careful planning, ongoing monitoring, and flexibility to ensure the mining operation remains safe, economically viable, and socially and environmentally responsible.

This study assesses the impact of fracture intensity, rock strength, and cave load on extraction level deformation and overall footprint capacity through a series of numerical scenario analyses. The analysis involves a submodeling approach with the discontinuum finite element numerical modelling method using a global mine scale model conducted in earlier studies. The boundary conditions for the submodels are derived from the global model to maintain the high similitude with displacements and the distribution of damage around excavations with resolution to a sub-bolt length scale. The paper will detail the model construction process and formulation of the constitutive model for the rock mass, defects, and ground support. The study's outcome is an overview of the upper- and lower-bound performance levels, representing the most and least favourable conditions for the tested scenarios.

1 INTRODUCTION

The success and sustainability of cave mining operations rely on adequate footprint management over the project's lifespan. The goal is to ensure safe and efficient mining operations while minimising geotechnical hazards and maximising resource recovery.

The footprint size and layout influence various aspects of cave mining operations, including the rock mass response, geotechnical challenges, ground stability, dilution control, and safety considerations (Melati et al., 2023; van As & Guest, 2020). Stability is a pivotal part of the design equation, with pillars serving as the primary support system for the production and undercut levels. Extraction activities, ground support design, and surrounding rock mass quality all shape the loading conditions on pillars. These loading conditions, in turn, determine the stress path within the pillars.

Managing pillar loading conditions effectively is crucial for maintaining pillar stability and overall mine safety. Pillars are subject to a complex evolution of stress paths during cave initiation, propagation, and maturation. Numerical simulations and computational methods help analyse stress changes in the pillars during each mining activity. These tools provide insights into how different factors affect the stress path within pillars and aid in optimising pillar design for stability and safety.

This paper will report on a numerical parametric study demonstrating the impact of cave load, rock mass strength, and fracture intensity on footprint capacity. Four footprint geometries are assessed under upper- and lower-bounds geotechnical conditions defined below:

- Upper Bound (UB) or most favourable ground conditions: rock mass with low DFN density and high rock matrix strength,

- Lower Bound (LB) or least favourable ground conditions: rock mass with high DFN density and low rock matrix strength,

2 METHODOLOGY

The study uses submodeling with an explicit finite element numerical modelling method to analyse stresses, strains, and displacements, including surface deformation effects within the area of interest. Submodelling is a numerical modelling technique used to enhance the accuracy and efficiency of simulations in complex systems where different scales of detail are required in different regions of the model. In this method, a coarse, global model (dubbed the donor model) is first constructed to capture the system's overall behaviour. Then, a refined, local model is built to capture the detailed behaviour in areas of particular interest. Starting with a large-scale, global model, submodelling allows focusing on a particular part of the model to obtain results with greater accuracy.

The simulation is 3D, with higher-order tetrahedral elements used for all volume elements. The displacement boundary conditions for the submodel are extracted from the results of the donor model, enabling a realistic stress path to be implemented. The submodel has the same number of modelling steps as the donor model, allowing the simulation to initialise and evolve as boundary conditions change gradually. This approach also eliminates sudden changes to boundary conditions, which may appear if the submodel was run at fewer steps.

2.1 Model geometry

The overall layout of the submodel geometry is shown in Figure 1, featuring a 5-by-5 drawbell arrangement with all key immediate excavations. This is part of a global model that simulated the behaviour of a block cave mine. The submodel boundary extends one drawbell further on all sides to minimise potential boundary effects on the results. The focal area of interest is a 3-by-3 drawbell layout positioned in the centre.

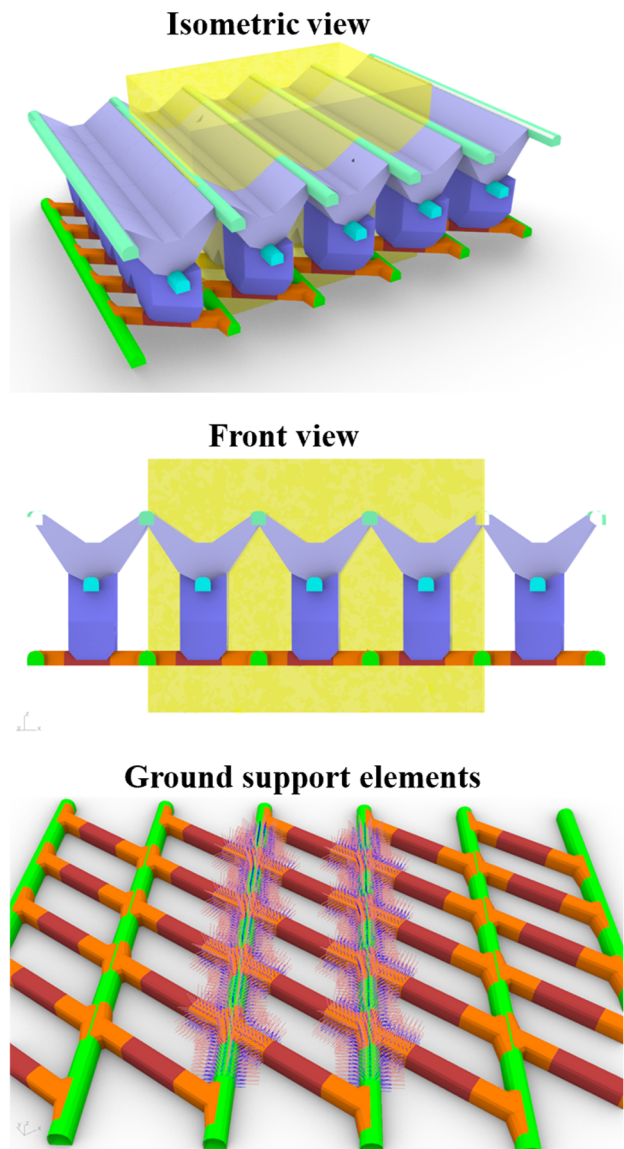


Figure 1 5x5 drawbells arrangement in submodel geometry; yellow box indicates the area of interest 3x3 drawbells setup.

Four footprint options are created by varying tunnel height (H) and width (W) and pillar dimensions, encompassing two levels for tunnel sizes (4.4 m W x 4 m H versus 5 m W x 4 m H) and two levels for pillar dimensions (30 m x 20 m versus 34 m x 22 m). The submodel geometries were constructed such that the location of the centre drawbell was maintained constant across all scenarios, thereby pushing the tunnels and drawpoint drives away from the centre.

Within the area of interest, the submodels incorporate ground support elements applied to

the extraction level drives (Figure 1). These elements consist of resin bars and cable bolts as primary and secondary support elements, as summarised in Table 1.

Table 1 List of ground support elements

| Excavations | Primary support: | Secondary support |
|-------------|-----------------------------------------------------|------------------------------------------------------------------------------------------------------------|
| Tunnels | 2.25 m long rock bolts 1 × 1 m 0.3 m from the floor | 4 m long cables 1 × 1 m 0.8 m from floor in the ribs 5 m long cables 1 × 1 m in the backs and shoulders |

Resin bars (fully grouted with solid steel bars) and cable bolts (fully grouted with steel strands) were explicitly built into the submodel as ‘beam elements’ with elastoplastic (von Mises-plasticity) properties. The lengths of beam elements are between 20 cm and 50 cm, and they have a circular cross-section, bending stiffness, and strain softening behaviour that is essential for modelling the bolts' failure.

All nodes of the beam elements are embedded in bulk rock, which means technically, no "slip" is allowed between the beam and the volume (rock) elements. The slip and failure of the grouting (or snapping of the bolt) is modelled through the appropriate beam properties (tensile strength vs. elongation), which were selected based on the measured pull-out force vs. pull-out distance. As those elements are an integral part of the model, the simulation considers force feedback from bolt elements to the rock and vice versa, meaning rock and bolts affect each other. More details on modelling ground support elements can be found in Dehkhoda et al., 2023.

2.2 Cave load conditions

The analyses are conducted under two distinctive geotechnical conditions, identified as the most and the least favourable environments for footprint stability:

- Upper Bound (UB) or most favourable conditions: low loading demand, low DFN density, high rock matrix strength,
- Lower Bound (LB) or least favourable conditions: high loading demand, high DFN density, low rock matrix strength,

The areas within the donor model satisfying the upper- and lower-bound conditions are identified, and the displacement data are extracted to assign them to the submodel boundary conditions. The two upper- and lower-bound setups also have mirrored undercut face orientation. The cave front in low-load demand scenarios is sub-vertical to the orientation of major principal stress. Meanwhile, in high-demand load scenarios, the cave front is subparallel to the orientation of the major principal stress. This is not a favoured orientation and is known to have a high risk of collapses and seismic hazards. The maximum cave load in the donor model was evaluated between 20 - 25 MPa.

2.3 Fracture intensity

The impact of fracture intensity is implemented using two distinct low and high-density discrete fracture networks (DFN). Each DFN set represented the local scale fracture planes (faults) and natural veining of the rock mass fabric. Considering the length scale of the problem (the target representative elementary volume [REV]) and to reduce meshing issues arising from small elements created by the intersection of the discrete fracture surfaces, a lower bound threshold was applied to the DFN sets, neglecting any fractures smaller than 2 m persistence. The homogenised continuum represented smaller defects. The size distribution of the built faults and veins are shown in Table 2. High-density DFN creates a blocky rock mass, whilst incorporating low-density DFN is a massive rock mass with random joints. In total, nearly 17,500 discrete fracture surfaces were explicitly built into the high-density submodel, whilst discrete fracture surfaces built into the low-density submodel were around 3,000.

Discrete fractures within the model are represented by combining cohesive elements to permit dislocations and separations on discontinuities while providing the correct kinematics of contact between the adjacent fracture surfaces. The main benefit is that the mechanics and kinematics of the contacts between the solid's continuous parts bound by cohesive elements are very well resolved and robustly solved, meaning the numerical solution is very stable. The representation of the stress-strain behaviour within rock parts need not be compromised to incorporate discontinuum behaviour.

Table 2 Size distribution of discrete fractures in low and high-density DFN.

| Size Range | Type A DFN | | Type B | |
|------------|------------|-------|--------|-------|
| | Low | High | Low | High |
| <3m | 64% | 81% | 66% | 79% |
| 3-5m | 27% | 15% | 27% | 16% |
| 5-10m | 7.2% | 3.67% | 6.39% | 4.38% |
| 10-20m | 0.86% | 0.14% | 0.73% | 0.23% |
| >20m | 0.04% | 0% | 0.08% | 0.01% |

2.4 Constitutive models and incorporated properties

The simulation components requiring a constitutive model can be divided into three categories:

- The continuum parts representing the intact rock or rock matrix between the discrete structure.
- Discrete structures representing the discontinuities and rock fabric.
- Rock and cable bolts.

The continuum parts are modelled as strain-softening dilatant materials using an extension of the Hoek & Brown failure criterion (Hoek & Brown, 2019) that considers strain softening as Levkovitch et al. 2010 described.

The incorporation of strain softening allows the material to soften, weaken, and dilate as strain increases. Each geotechnical domain is defined by its material properties, and all parameters for each rock type can vary at different rates concerning strain changes, including the dilatancy parameter. This allows approximation of very complex stress-strain behaviour.

The derived REV scale HB material properties for the upper and lower bound rock matrix strength scenarios are given in Table 3. The idealised stress-strain curve, including post-peak response, is also shown in Figure 2.

Table 3 REV scale material properties

| | ρ [kg/m ³] | UCS [MPa] | GSI | Level | ϵ_p [%] | E [GPa] | ν | s | m_b | a | dilation |
|-------|--------------------------------|--------------|-----|-------|------------------|------------|-------|---------|-------|------|----------|
| Low | 2700 | 110 | 68 | PEAK | 0% | 28.7 | 0.27 | 2.1E-02 | 4.69 | 0.50 | 0.28 |
| | | | 51 | TRANS | 1.44% | 24.4 | 0.27 | 1.4E-03 | 1.68 | 0.51 | 0.21 |
| | | | 44 | RES | 10.53% | 18.6 | 0.27 | 9.1E-05 | 0.32 | 0.51 | 0.10 |
| Upper | 2700 | 130 | 74 | PEAK | 0.00% | 30 | 0.28 | 4.3E-02 | 5.50 | 0.50 | 0.33 |
| | | | 56 | TRANS | 1.56% | 25 | 0.28 | 2.6E-03 | 1.91 | 0.50 | 0.25 |
| | | | 48 | RES | 9.25% | 19 | 0.28 | 1.8E-04 | 0.39 | 0.51 | 0.12 |

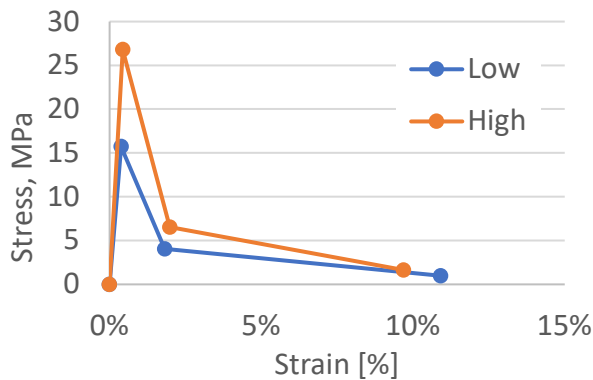


Figure 2 REV scale rock matrix uniaxial σ - ϵ curve built into the model.

Discrete structures have been implemented as cohesive elements, and the Hoek & Brown failure criterion was used to determine 3D yield surfaces for discrete structures. The mechanical

properties of the discrete structures built into submodels are listed in Table 3. As can be seen, size-dependent strength properties were developed for the fault type DFN in the dense option to prevent unexpected numerical slips along the fractures immediately after undercutting. This issue stemmed from the extensive number of large fracture surfaces and associated interconnectivity within the system, which, as a result, leads to large slips when confinement is reduced.

Rock bolts and cable bolts were defined as elastic, perfectly plastic materials based on the von Mises yield criterion. Its properties were adopted from in situ pull-out tests conducted on-site. Table 5 shows the incorporated properties for rock and cable bolts within the submodel.

Table 4 Input properties for structural defects

| DFN | Persistence | | Tensile strength, MPa | Cohesion, MPa | Friction angle, deg | Compressive strength, MPa |
|--------------|-------------|----------|-----------------------|---------------|---------------------|---------------------------|
| High-Density | Type A | 20m plus | 4.1 | 10.5 | 35.0 | 40.5 |
| | | 10-20m | 3.2 | 8.2 | 35.0 | 31.5 |
| | | 5-10m | 2.7 | 7.8 | 30.0 | 27.0 |
| | | 3-5m | 1.4 | 3.9 | 30.0 | 13.5 |
| | Type B | All | 0.6 | 1.5 | 25 | 4.7 |
| Low Density | Type A | All | 4.5 | 11.25 | 40 | 48 |
| | Type B | All | 0.6 | 1.5 | 25 | 5 |

Table 5 Implemented yield criterion for rock and cable bolts

| Type | Diameter (mm) | Yield strength (MPa) | Displacements at yield (mm) | Stiffness (GPa) | Poisson's ratio |
|-------------|---------------|----------------------|-----------------------------|-----------------|-----------------|
| Cable bolts | 15.2 | 1,860 | 25 | 40 | 0.3 |
| Rock bolts | 22.1 | 690 | 15 | 67 | 0.3 |

3 RESULTS AND ANALYSES

The performance of four footprint geometric scenarios under upper- and lower-bound ground and cave load conditions are compared in the sections below. The upper-bound (UB) and

lower-bound (LB) scenarios represent the most and the least favourable ground conditions. The UB incorporated a high-strength rock matrix, low-density DFN, and relatively favourable cave load demand, whilst the LB featured a low-strength rock matrix, high-density DFN, and

unfavourable cave load demand. The UB submodels' boundary was exerted by ~5 m-10 m vertical downward displacement, based on data from the donor model. The downward vertical displacement applied to the LB submodels's boundary was consistently over 15 m.

3.1 Mining-induced stress and associated damage

Stress redistribution and damage after the undercut are shown in Figure 3 and Figure 4 for selected model frames at various cave loads.

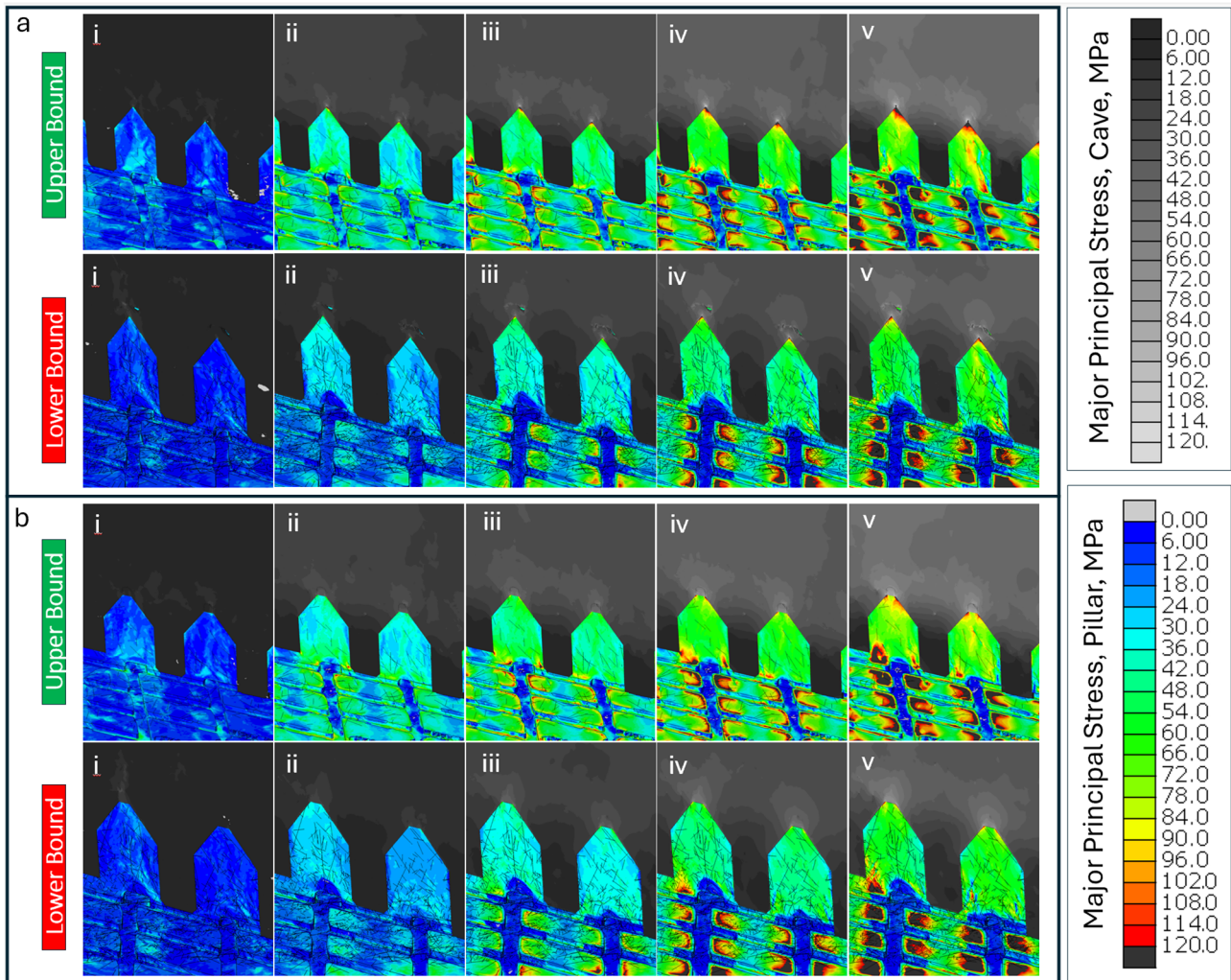


Figure 3 Evolution of major principal stress in the extraction level and the pillars. a) 4.4 m width x 4 m height tunnels, 30 m x 20 m pillar dimension. b) 5 m width x 4 m height tunnels, 34 m x 22 m pillar dimension. i. immediately after undercut, ii. average cave load=10 MPa, iii. average cave load=20 MPa, v. average cave load=30 MPa, vi. average cave load=40 MPa. Upper Bound: strong rock matrix, low-density DFN. Lower Bound=weak rock matrix, high-density DFN.

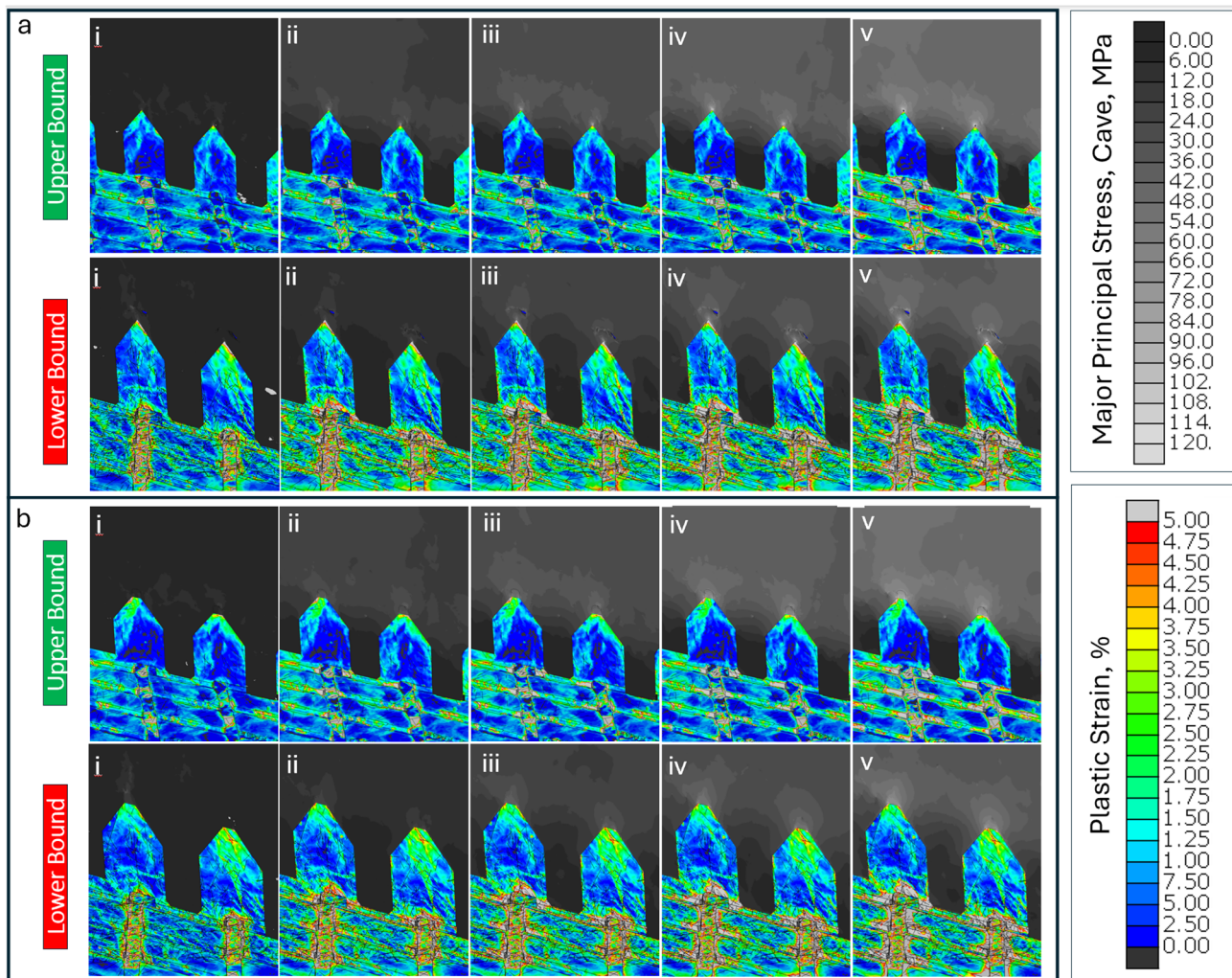


Figure 4 Evolution of damage in the extraction level and the pillars with cave load. a) 4.4 m width x 4 m height tunnels, 30 m x 20 m pillar dimension. b) 5 m width x 4 m height tunnels, 34 m x 22 m pillar dimension. i. immediately after undercut, ii. average cave load=10 MPa, iii. average cave load=20 MPa, v. average cave load=30 MPa, vi. average cave load=40 MPa. Upper Bound: strong rock matrix, low-density DFN. Lower Bound=weak rock matrix, high-density DFN.

The results show that:

- Destressing after the undercut is similar for the UB and LB scenarios; however, stress relaxation in lower-bound scenarios leads to more significant damage to the extraction level. This damage is structurally controlled, meaning the governing mechanisms are shear/dilation on the DFN surfaces.
- The damage around the tunnels depends highly on the incorporated DFN, meaning that a slightly different DFN setup would create different block shapes and conditions that may or may not lead to the same conclusions. The nature of the induced damage was also determined by the geometry of the DFN (shape and size of the blocks/wedges). A high-density DFN creates a significantly larger number of blocks around the excavations at risk of dislocation after stress relief, leading to rockfall or dilation on the DFN surfaces. Therefore, the DFN assumptions must be confirmed by mapping the excavations.
- In LB scenarios, minor damage first evolves around the bullnoses and tunnel walls and extends to the backs as caving progresses. In the UB scenarios, though, with stress relaxation and loss of confinement, damage first develops at the back of the large

excavations and then grows to the tunnel walls as the cave load increases.

- As the cave load increases, stress within the pillars rises. Once the cave load exceeds 20 MPa, the pillar stresses reach over 120 MPa. This corresponds to increased accumulated plastic strain around the tunnels and the appearance of shear bands localised on persistent defects within the pillars.

3.2 Pillar performance

The effect of pillar size on the evolution of stress and strain and overall pillar performance is assessed quantitatively using statistical analyses conducted on data extracted from the model. For this purpose, stress and strain within the pillar and the cave were sampled randomly at every model step. More than 5000 data points were extracted from the centre pillars to create representative data sets. Cave loads were sampled at over 280 points (Figure 5). For ultimate comparison, mean values were used.

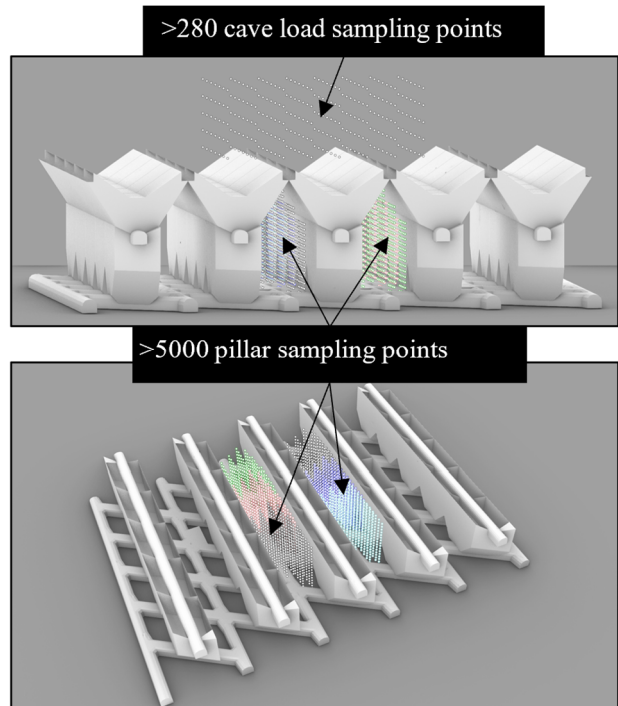


Figure 5 Overview of data extraction locations for quantitative stress and strain analyses within the pillars.

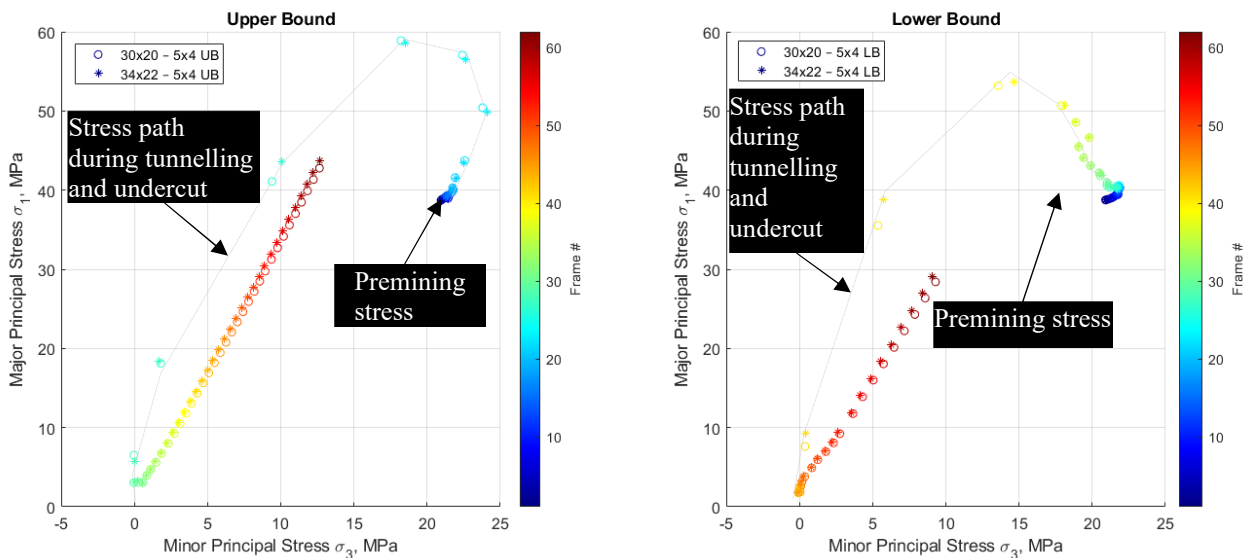


Figure 6 Evolution of major principal stress within the cave during cave establishment.

The evolution of major and minor principal stresses within the cave is compared in Figure 6 under the upper- and lower-bound ground conditions. The plot presents the full stress path, from the in-situ pre-mining stress state to excavation-induced stresses to destressing due to undercuts, and finally, a consistent rise in cave load during production. As can be seen, footprint

layout has a minor impact on the cave load variation. The results show that:

- Undercut-related destressing occurs faster under LB conditions than under UB conditions. The LB stress state within the cave at the end of the undercut is slightly lower than the UB.

- The rate of increase in cave load during production is similar for both scenarios.

Pillar performance is assessed based on the evolution of stress and strain within the pillars during the undercut and cave establishment (Figure 7). As expected, results confirm that the large pillar (34 m x 22 m) exhibits a higher load capacity than the small pillar (30 m x 20 m). However, confinement loss reduces this capacity significantly during and immediately after undercutting. This effect is exacerbated in large pillars when fracture intensity is high. The pillar regains its load-bearing capacity as the vertical load increases with the production and establishment of the cave.

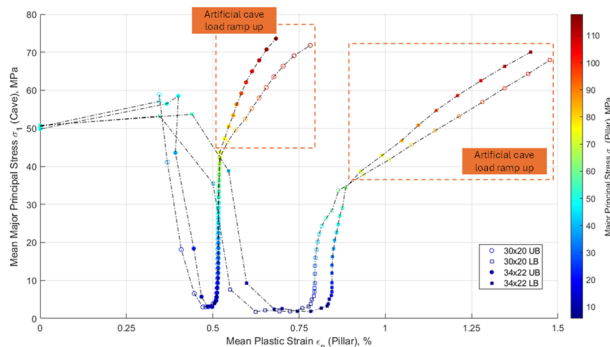


Figure 7 Impact of pillar size on stress and plastic strain evolution within pillars.

Overall, the impact of upper- and lower-bound ground conditions on pillar performance is more pronounced than the footprint geometric layout (Figure 7). Pillars under the LB ground conditions are softer and can undergo more plastic strain and damage than pillars under UB conditions at similar cave loads. Dense DFN is the major contributing factor as they are more susceptible to slip with confinement loss. Note that the rock matrix is also weaker in LB than in UB (halved).

3.3 Wall-to-wall closure

The study also investigates the influence of cave load and LB and UB ground conditions on wall-to-wall closure (convergence) along the extraction level (EL) excavations. In these analyses, the cave load was artificially ramped up to impose collapse scenarios within the model. The load curve is shown in Figure 6.

Numerical convergence data are generated by measuring the distances between set points on the opposing walls of the excavations, such as wall-to-wall and roof-to-floor distances. The statistical distribution of forecast convergence at specific cave loads is presented in Figure 8 for two pillar sizes and both UB and LB ground conditions. The impact of tunnel size on convergence is also illustrated in Figure 9 for the LB scenarios.

As anticipated, closure increases with cave load and EL excavations exhibit more significant displacements under LB conditions than UB conditions. The results reveal:

- At low cave loads, the impact of tunnel size is more pronounced, so large tunnels are slightly worse off. As cave load increases, having large pillars becomes an advantage in controlling closure. During the transitioning period, the performance of a large pillar/small tunnel is similar to that of a small pillar/large tunnel.
- Small pillar and large tunnel scenarios are more likely to experience excessive closures (>200 mm). Under UB conditions, less than 2% of the excavations experience larger than 200 mm closure when the cave load is below 40 MPa. Rehab is expected where closure exceeds 200 mm.
- Tunnels in the LB scenario experience significantly larger closures than those in the UB scenario (Figure 9). At a cave load of 30 MPa, the percentages of tunnels exceeding the 200 mm threshold are:
 - ~17% in 30 m x 20 m – 4.4 m x 4 m layout.
 - ~25% in 30 m x 20 m – 5 m x 4 m layout.
 - ~15% in 34 m x 22 m – 4.4 m x 4 m layout.
 - ~22% in 34 m x 22 m – 5 m x 4 m layout.
- These are mainly at the corners and backs of large excavations and initiated by blocks or wedges. At these levels of movement, experience suggests that damage to the bolts would result in a loss of support capacity at the point of damage.

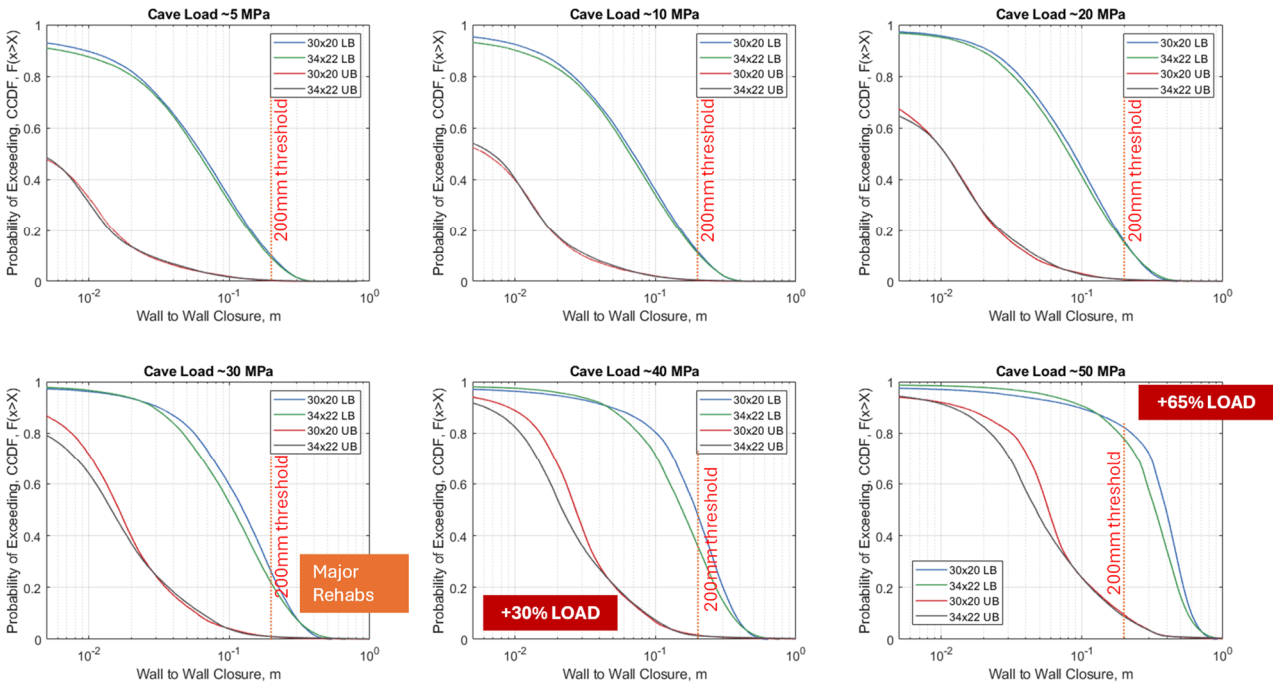


Figure 8 Impact of pillar size and upper- and lower-bound conditions on tunnel closure at various cave loads. Tunnel size: 5 m W x 4 m H.

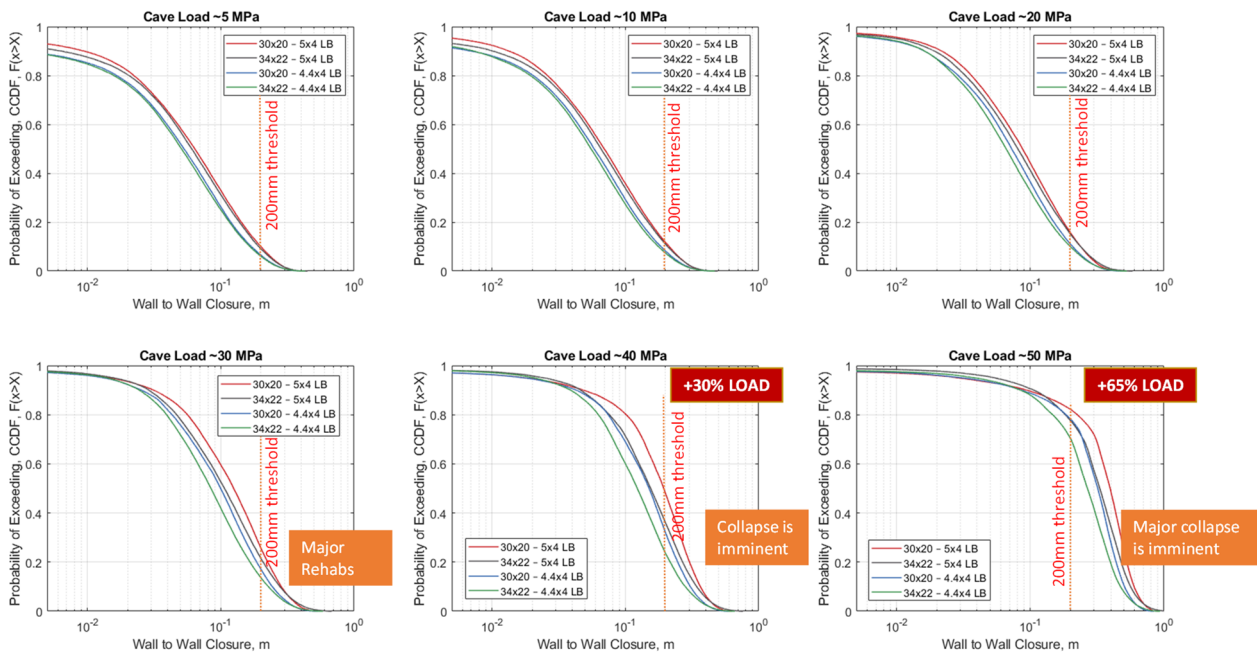


Figure 9 Impact of footprint layout on EL wall closure at selected cave loads – LB conditions.

4 CONCLUSIONS

This paper reports on the outcome of a numerical parametric study that assesses the impact of cave load, rock mass strength, and fracture intensity on tunnel deformation and overall footprint capacity in the discontinuous rock mass. Four different footprint geometries were evaluated under two geotechnical settings, characterised as below:

- Upper Bound (UB) or most favourable conditions: low loading demand, low DFN density, high rock matrix strength,
- Lower Bound (LB) or most favourable conditions: high loading demand, high DFN density, low rock matrix strength,

The simulations confirm the observations that the tunnel damage is initiated by the dislocation of blocks and bulking due to loss of confinement after undercut. The geometry of the incorporated DFN drives the nature of the induced damage. Hence, the DFN must be confirmed with the mapping of the excavations.

Similarly, pillars suffer plastic strain and damage with the undercut, momentarily losing load-bearing capacity with confinement loss. The magnitude of damage is significantly larger under LB ground conditions than in UB. Dense DFN is the major contributing factor as they are more susceptible to slip with confinement loss. Note that the rock matrix is also weaker in LB than in UB (halved). Pillars regain capacity as load builds with continued production and cave establishment. As anticipated, large pillars and small tunnel combinations can take a higher load and are less susceptible to excessive strain accumulation.

This type of discontinuum modelling calls for accurate mechanical characterisation of the fracture surfaces. The study proved the sensitivity of the outcome to the geometric and mechanical properties of the incorporated DFN. Experiments such as direct shear tests can be used to determine their representative properties. Stress cells installed in pillars throughout the cave footprint would also enable the load history to be measured during cave flow trials and draw

experiments. Stress cells combined with open holes to assess rock mass damage and extensometers to measure movement would enable pillar behaviour and stability to be assessed and numerical model forecasts to be validated.

REFERENCES

- Dehkhoda, S., Reusch, F. & Putzar, G. (2023). A numerical approach for a displacement-based ground support capacity consumption forecast, In J Wesseloo (ed.), *Ground Support 2023: Proceedings of the 10th International Conference on Ground Support in Mining*, Australian Centre for Geomechanics, Perth, pp.573-590, https://doi.org/10.36487/ACG_repo/2325_39.
- Hoek, E. & Brown, E. T. (2019) The Hoek–Brown failure criterion and GSI – 2018 edition. *Journal of Rock Mechanics and Geotechnical Engineering*, vol. 11, no. 3, pp. 445–463.
- Levkovitch, V., Reusch, F. & Beck, D. (2010). Application of a non-linear confinement sensitive constitutive model to mine scale simulations subject to varying levels of confining stress. In J Zhao, V Laboure, J-P Dudt & J-F Mather (eds), *Rock Mechanics in Civil and Environmental Engineering*, CRC Press, Boca Raton.
- Melati, S., Wattimena, R. K., Sahara, D. P., Syafrizal; Simangunsong, G. M., Hidayat, W., Riyanto, E. & Felisia, R. R. S. (2023). Block Caving Mining Method: Transformation and Its Potency in Indonesia', *Energies*, vol. 16, no. 9. <https://doi.org/10.3390/en16010009>.
- van As, A. & Guest, A. (2020). The design & operating philosophies of panel vs block caving. In R Castro, F Báez & K Suzuki (eds), *MassMin 2020: Proceedings of the Eighth International Conference & Exhibition on Mass Mining*, University of Chile, Santiago, pp. 207-220, https://doi.org/10.36487/ACG_repo/2063_10.